Beyond actuator line arrays in active flow control studies: Lessons from a genetic algorithm approach

Fernando Zigunov, * Prabu Sellappan, and Farrukh Alvi
Florida Center for Advanced Aero-Propulsion (FCAAP), Department of Mechanical Engineering, FAMU-FSU College of Engineering, Tallahassee, Florida 32310, USA

(Received 23 February 2021; accepted 10 August 2021; published 23 August 2021)

This study explores the problem of optimal spatial placement of microjet actuators for flow control in a canonical bluff body of relevance to the aerodynamics community, namely, the slanted cylinder with a slant angle of 45°. The solution found by a genetic algorithm whose goal function is to reduce aerodynamic drag (achieving 10.6% reduction at $\mathrm{Re}_D = 100\,000$) challenges the intuitive and, to date, most commonly followed *de facto* standard of using line arrays of steady microjet actuators to control a flow field. This study provides strong evidence that line arrays are not the optimal approach for active flow control of this bluff body wake, since most of the jets in the line array were neutrally, or even negatively, contributing to the goal function of drag reduction. Further observations of the flow physics with surface flow visualization and particle image velocimetry unveil two key mechanisms that were leveraged by this automated approach: First, a shrinkage of the separation bubble at the leading edge of the slanted surface appears to be strongly related to the very strong energization of the boundary layer just upstream of the separation due to microjets in crossflow being applied in tandem. Second, a wavelike perturbation that appears to be related to an increased wandering of the vortex pair formed in the far field of this wake is also observed. Although this study employed steady microjet actuators, the lessons learned can potentially be extended to other actuation mechanisms commonly used for active flow control. The results obtained demonstrate the spatial sensitivity problem is one that, despite its complexity and challenges in physical implementation, is worthwhile considering in active flow control studies.

DOI: 10.1103/PhysRevFluids.6.083903

I. INTRODUCTION

Active flow control is a technology that has the potential to have an impact on how fluid dynamical systems are engineered [1]. In particular, blowing through small holes on the aerodynamic surfaces has been shown by many researchers to significantly alter the characteristics of the near-surface flow [2,3], which can cascade into dramatic changes in the mean flow field and its unsteady characteristics, affecting relevant engineering quantities such as aerodynamic drag [4–8] and noise production [9,10] and improve the operational envelope of aerodynamical systems [11–13].

One of the many challenges that make implementation of active flow control based solutions difficult in real engineering flows is related to the problem of placement of these microactuators. An aerodynamic system with microactuators relies on the multiscale nature of the Navier-Stokes equations to leverage changes in properties of the smaller scales of the flow (such as boundary layers and shear layers) to perturb and modify the larger scales of a flow field, producing measurable

*Corresponding author: fzigunov@fsu.edu

changes in integral quantities of interest, such as aerodynamic drag. This working principle demands a greatly increased resolution from computational models that make it prohibitive, at the computational capacity of contemporary systems, to simulate a large number of spatial patterns of microjet actuators. With contemporary computational systems, simulating a single microjet in crossflow at application Reynolds numbers while capturing the relevant length and time scales is already a significant undertaking [3,14]. Due to these limitations, computational techniques are currently under development to tackle the spatial sensitivity problem [15–20] and can be instrumental to inform experimental endeavors in this topic. However, it is arguably unclear whether techniques based on small perturbations of a flow field will lead to physically realizable or even effective actuation schemes, given an integral part of the working principle of actuators used in active flow control is to leverage the nonlinearities of a flow to cause large-scale changes in the flow field.

Therefore, it is in experimental studies that one can more realistically and more confidently assess the effectiveness of a given actuation scheme, always taking into consideration that wind tunnel experiments have limitations of their own. Obviously, the costs related to experimental studies limit the number of combinations that can be explored. The limited number of experiments and the lack of computational tools to predict the best actuation locations turns the experimental search into a lengthy trial-and-error process, where actuator placement decisions require experience and intuition from the experimentalist. Predicting a location for a microjet-in-crossflow actuator that causes even a measurable change in a practical curved surface of a bluff body, such as the ones employed in ground or flying vehicles, is not trivial. This is possibly the reason it is more common to encounter studies on simplified, sharp-edged models such as the Ahmed body, ramps, and cavities, as well as unswept wings, where the location of the flow separation is mostly dictated by the model geometry or can be predicted with reasonable accuracy. Experimental studies on curved bluff body surfaces at the current stage of development must be parametric in spatial dimensions, which is deemed to be expensive due to the necessity of changing the model, restarting the wind tunnel, among other practical issues. A recent study by the authors [21], however, demonstrates that enabling a computer to access different actuator locations via multiple channels of pneumatic solenoids is feasible and affordable with state-of-the-art technology. In this context, further advancements in measurement, processing and channel count increase (for example, via MEMS actuators [22]) can empower experimental studies to bring active flow control technology to engineering applications by better tackling the spatial sensitivity problem.

There is much to be learned from optimization studies that involve actuator spatial location. As the title of this study suggests, it is an overwhelmingly common experimental practice to use line arrays of microjets, line-shaped blowing/suction slots, and other actuation methods in active flow control studies in both streamlined geometries [12,23–27], as well as bluff bodies [4–7,28–34]. Flow control studies where the actuators do not form a line pattern are much less ubiquitous [8,35], to the knowledge of the authors. Line arrays are a natural choice, since one might reason that the counter-rotating vortex pair produced by a single microjet immersed in a boundary layer has limited spanwise reach with respect to its streamwise effect due to the convective nature of the flows that are the subject of such studies. This is a sensible observation when the microactuator is immersed in an attached flow; however, when the actuator is under a separated shear layer, it is surrounded by a region of the flow with much lower velocities and the flow field resembles more of a jet in a quiescent medium, given the jet velocities are much larger than the velocities under the separation zone. Fernandez [2] showed that there are optimal parameters for microjet actuators arranged in line arrays; however, there is nothing inherently optimal about the line array configuration itself, especially in three-dimensional bluff body wakes and flows over swept wings. On the other hand, configurations of microjets other than simple line array shapes are much more difficult to engineer because the parameter space becomes combinatorial.

Motivated by this unresolved issue, a recent study by the authors [21] demonstrated the development of an experimental system that is capable of optimizing the actuator spatial pattern utilizing a genetic algorithm (GA) approach, inspired by the recent experimental applications of GAs in flow control [36–38]. The device developed in [21] was able to achieve a drag reduction

of 10.5% in the wake of a cylinder aligned with the flow with a slanted afterbody. The wake of the cylinder with a slanted afterbody displays two possible flow regimes with different topologies, conjectured by Morel [39] based on drag measurements and observed experimentally with flow visualization techniques by Zigunov [40], with the presence of hysteresis at low Reynolds numbers ($\mathrm{Re}_D < 60\,000$). The vortex-dominated regime has been extensively studied in the literature [41–44] and is characterized by a pair of strong counter-rotating vortices in the near-wake, above the slanted surface. The wake state has been characterized in only a few studies [40,45] and displays a fully separated bluff body wake, with base pressure recovery and reduction in drag. Both flow regimes are stable states, meaning there is no switching between the flow regimes as a function of time in this wake. In this study, the flow regime of the baseline, uncontrolled flow is the vortex-dominated regime.

The drag reduction achieved in the slanted cylinder wake by the GA approach was an improvement by almost a factor of 3 using about half as many jets, when compared to actuator line arrays deployed in the same study [21]. This achievement was possible only due to the flexibility of the experimental platform developed, which did not start with the premise that the actuation pattern should be a line array. The result obtained, in fact, was an actuator distribution much different than a line array. The current study will extend the results obtained, by closely examining the impact of the best actuator patterns on the flow physics with advanced flow diagnostics in order to understand the fundamental mechanisms that the nonintuitive configuration might have exploited and their differences in comparison to the more traditional, but less effective line array configuration.

II. EXPERIMENTAL SETUP

A. Details of the aerodynamic model and facility

The experiments presented herein constitute a follow-up study on the encouraging results obtained by the genetic algorithm (GA) study presented in [21]. Our prior study focused on the more practical, technical aspects of the build: Design, hardware implementation and implementation of the GA. As previously mentioned, here we focus on understanding the differences in the flow physics between the GA solution and the traditional linear array. Both studies were performed at the Florida Center for Advanced Aero-Propulsion (FCAAP), in the Low Speed Wind Tunnel (LSWT) facility. The facility is capable of free stream velocities between 2.5 m/s and 70 m/s, and the experiments reported in this work were all performed at a free stream velocity of $V_\infty = 10.3$ m/s. This free stream velocity corresponds to a diameter-based Reynolds number of $\mathrm{Re}_D = 100\,000$, where $D = 146.05$ mm is the diameter of the slanted cylinder model depicted in Fig. 1(a). The slanted cylinder is a canonical bluff body used for studies of the wake produced by an aircraft fuselage, and its most important parameter is the slant angle ϕ, which defines the flow regime along with the model Reynolds number [39]. The slant angle employed in this study, $\phi = 45^\circ$, produces a counter-rotating vortex pair in its far field wake at the Reynolds number tested. A simplified depiction of the flow topology of this model is given in Fig. 1(b), based on the stacked stereoscopic PIV measurements performed by Zigunov *et al*. [42] as well as evidence provided by other researchers [41,44,46,47].

In Fig. 1(a) some of the internal details of the experiment performed in [21] are also shown. The experiment had individual computerized control over 59 pneumatic channels inside the model, which enabled detailed study of the influence of individual groups of microjets. Further details of the implementation of the jet array are given in Sec. III and [21].

B. Flow diagnostics

One of the goals of this study is to gain a deeper understanding of what mechanisms were leveraged by the spatial configurations that were effective in reducing the circulation of the far field vortex pair. To achieve this, targeted experiments were conducted to explore the changes promoted

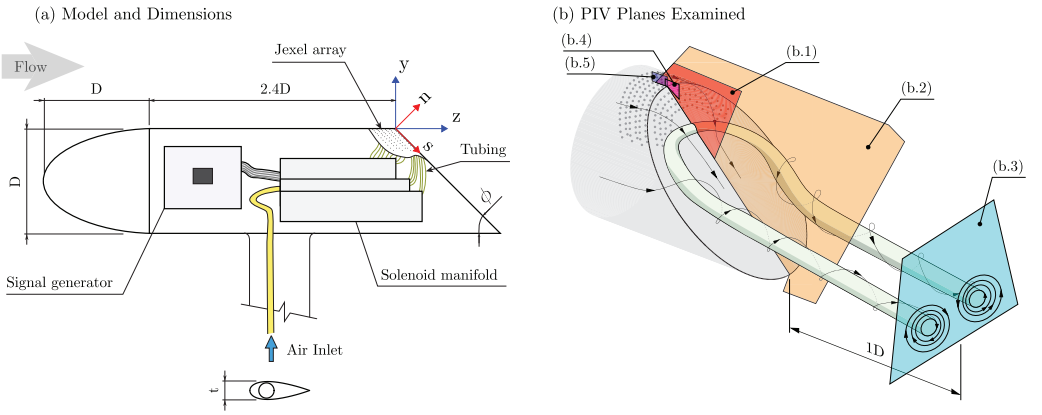

FIG. 1. (a) Model dimensions and simplified schematic of the internal mechanism used to actuate the microjets with control over every *jexel*. Blue and red coordinate systems mark the origin used in the Results section. (b) Schematic of the baseline flow field interrogated as learned from [42] and specific planes used in this study.

by active flow control to the main flow features in this flow: the separation bubble and the vortex pair. These features were interrogated with particle image velocimetry and surface oil flow.

1. Particle image velocimetry

Five distinct particle image velocimetry (PIV) planes were examined in this study. Planar PIV was performed at the planes shown in Fig. 1, (b.1), (b.2), (b.4), and (b.5), where plane (b.1) focused on understanding the dynamics of the separation bubble, plane (b.2) was directed at capturing any effects on the trailing edge shear layer dynamics, and planes (b.4) and (b.5) focused on the boundary layer and separation bubble effects. The planar PIV setups employed a commercial LaVision solution with a single LaVision sCMOS camera fitted with a 135 mm Nikkor lens for plane (b.1), a 50 mm Nikkor lens for plane (b.2), and a 200 mm Nikkor lens adapted with a 2× teleconverter for planes (b.4) and (b.5), to achieve a magnification of about $s_{\text{object}}/s_{\text{sensor}} = 0.77$. The illumination was provided by a Quantel Evergreen Nd:YAG double-pulse laser with a pulse energy of 200 mJ, expanded to a sheet of appropriate size and thickness of approximately 2 mm. Capture of the PIV images was performed at 15 Hz, and postprocessing was done with LaVision DaVis 8.4, with 3 passes of a 32 × 32 px correlation window with 75% overlap, resulting in a vector spacing of 0.55 mm/vec for plane (b.1), 0.91 mm/vec for plane (b.2), and 43.5 μm/vec for the high magnification planes (b.4) and (b.5).

Plane (b.3) shown in Fig. 1 is a spanwise plane located at $z/D = 2$, or 1 diameter away from the trailing edge of the model. This plane contains the vortex pair and part of the shear layer produced by the trailing edge, and was captured with a stereoscopic PIV (SPIV) setup that involved two LaVision sCMOS cameras. The cameras were looking from upstream of the model and were fitted with a Nikkor 50 mm lens and a Scheimpflug adaptor for correction of the angle of the focal planes. The SPIV capture rates, laser energy, and configurations were the same as previously described for planar PIV, which given the position where the cameras were placed resulted in a vector spacing of 0.62 mm/vec. The uncertainty of the mean vectors obtained was <2% for both techniques.

2. Surface oil flow

Surface oil flow visualization is a simple technique that provides a great amount of insight into the topology of the flow studied. It is particularly useful for active flow control studies, since qualitative

changes in the flow field can be observed by toggling the microjets on/off with the wind tunnel running.

In order to observe the surface patterns, a thin layer of SAE 0W5 engine oil was spread over the model surface with the help of a paper towel, and green particles of ground chalk were spread over the surface with a sieve. A thin oil layer is crucial at the slant angle used, since it is important that the effect of the gravitational force is minimized. The particles would act as seed points for the green dye, which displays fluorescence under ultraviolet (UV) light. Commercial "black light" light bulbs were used as the source of UV during the experiments. The flow of the oil over the surface would then slowly carry the fluorescent dye with it, revealing the mean surface flow topology. This process, however, is very slow under the low free stream velocity of the experiment, especially in regions where shear stress is low at the surface. A time-lapse movie of approximately 30 minutes for each case was taken to examine the evolution of the pattern, which helps in determining the direction of the oil flow streamlines. The time-lapse footage is compiled in the Supplemental Material [48], since it provides very useful insights and presents evidence of the effectiveness of the actuation strategies.

III. GENETIC ALGORITHM IMPLEMENTATION AND OVERVIEW OF PAST RESULTS

In a past study [21], a platform to automatically explore spatial patterns of microjets in crossflow was developed with the objective of finding effective microjet configurations in the nontrivial context of the slanted cylinder wake. The platform consisted of an array of 100 Matrix Pneumatix DCX.321.1E3C2.24 solenoid valves, individually addressable by an USB-Serial interface driver developed by the authors and available as an open-source project [49]. Fifty-nine of the solenoids were connected in the experiment to 59 groups of four microjets (herein denominated a *"jexel,"* short for "jet *pixel,*" as each pneumatic channel is used to form a spatial pattern in a similar way a *pixel* is used to form an image). Then a genetic algorithm (GA) was used to explore these spatial patterns, by experimentally measuring the cost function J for each individual pattern. The details in the implementation of the GA are provided in [21], and are also described in the Appendix. The cost function J is defined as

$$J = \frac{\Gamma_{\text{jexel}} - \Gamma_{\text{baseline}}}{\Gamma_{\text{baseline}}} = \frac{\Delta\Gamma}{\Gamma} \propto \frac{\Delta C_D}{C_D}, \tag{1}$$

$$\Gamma = \int_C \vec{V} \cdot \vec{d}s, \tag{2}$$

where the circulation of the right-hand vortex produced by the flow over the slanted cylinder Γ is approximated by traversing a four-hole probe around a circle centered at the vortex core with an appropriate radius ($r/D = 0.274$) and number of points ($n_{pts} = 40$). The circulation is used as a reliable proxy for drag, as shown by Bulathsinghala *et al.* [44]. In the case of drag reduction, J is to be a negative number and a minimization algorithm will accomplish the goal of minimizing drag. The approach of measuring circulation, instead of directly measuring drag, was chosen due to its lower measurement uncertainty, an essential ingredient for the success of an optimization strategy.

A summary of the results obtained in [21] is presented in Fig. 2, which serve as a starting point for the discussion presented herein. A physical view of the model used and the *jexel* is presented in Figs. 2(a) and 2(b). In Fig. 2(b) the *jexel* is presented in two states as viewed from inside the model. In the left of Fig. 2(b), the *jexel* cavity is closed and connected with a 0.063-inch pneumatic tube that connects to a solenoid valve. The right-hand side of Fig. 2(b) shows the open *jexel* cavity, revealing each *jexel* consists of four round jets of 0.4 mm diameter each, spaced 6 mm apart in a square arrangement. In the study performed in [21], an identical part made through the process of stereolithographic three-dimensional (3D) printing (SLA) was employed; however, this model was upgraded for the results shown in the present work to a fully machined model. The 3D CAD of the actuator section was exactly the same for both studies to ensure maximal comparability between the results. Overlapping measurements were performed in the two models for about ∼500 different

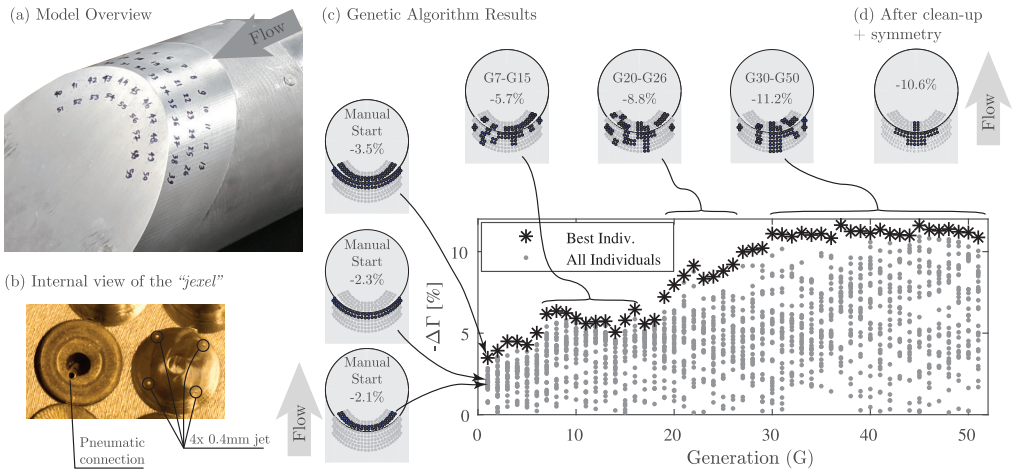

FIG. 2. (a) Overview of the setup used for the reconfigurable jet array and (b) detail of the *jexel* viewed from inside of the model, showing how each group of four microjets are grouped in a cavity. (c) A summary of the progress the GA was able to achieve by starting with manually selected line array configurations. (d) The symmetric, "cleaned-up" configuration derived from the GA result.

jexel patterns encountered by the GA, with agreement within the 2σ uncertainty of the experiment ($\pm 1\%$ of Γ_{baseline}).

Figure 2(c) presents a summary of the progress that was possible with this setup through the use of the GA when the SLA part was used. The manual starting configurations, consisting mostly of line arrays, were fed into the starting population of the GA. In about 30 generations, a converged solution was achieved. The algorithm was run for 20 more generations to confirm the solution was indeed converged. Although the GA had access to pulsing the jets at frequencies between 1 and 200 Hz, it was found [21] that the most effective solution was open-loop steady (DC) blowing. Thus, this study will focus on DC blowing solutions only.

An iterative clean-up process was then applied to the GA solution [best of G51] by implementing a hybrid breadth-first/depth-first search algorithm, whose implementation details and pseudocode are provided in the Appendix. This procedure was applied to remove *jexels* that were randomly placed by the GA but had little to no contribution to the performance of the solution. The clean-up procedure also improved the interpretability of the patterns identified. The clean-up algorithm can be briefly described as follows.

Starting with the solution, one *jexel* was deactivated temporarily and the cost function would be measured. For example, if the solution consisted of N *jexels*, this process would be performed N times, and each time a permutation with $N-1$ active *jexels* would be examined. This procedure enables one to assess which of the N *jexels* in the configuration is the least important. A *jexel* is deemed as the least important if it either increases the cost function or it does not reduce it as much as the remaining *jexels*. Mathematically, we find $\text{argmin}(J_n[m])$ and deactivate the corresponding mth *jexel*. Then we repeat the process, now with $N-1$ *jexels*. This is repeated until there are no *jexels* left to deactivate.

A set of eight *jexels* was selected as minimally important to the configuration. A PIV study [21] revealed that the important *jexels* exploited the asymmetry of the measurement (i.e., only the right-hand vortex was measured). A symmetric configuration was then explored, which is displayed in Fig. 2(d). This configuration will be explored in further detail in this study, and will be hereafter called the *GA solution*. All *jexel* patterns detailed in the following sections of this paper will employ DC blowing at the optimal back-pressure of $P_S = 52$ kPa, which corresponds to a blowing ratio of $B = V_{jet}/V_\infty = 7.3$.

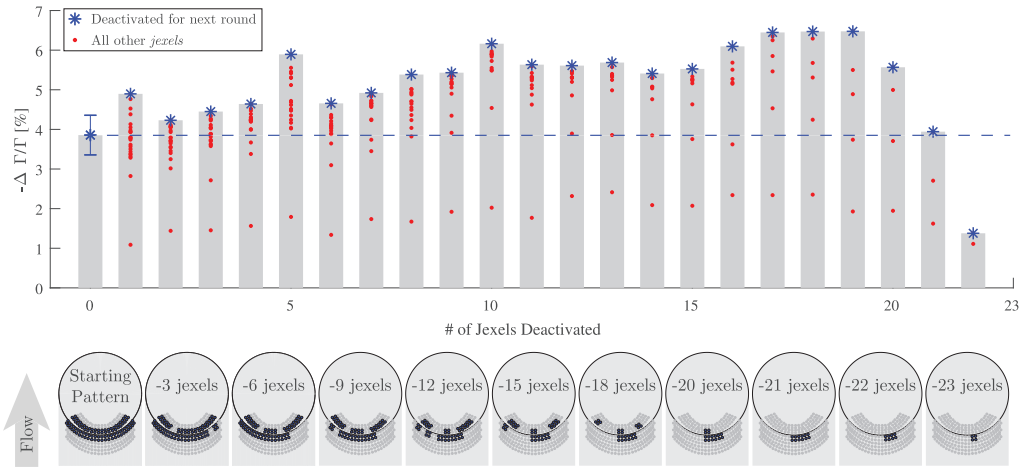

FIG. 3. Iterative *jexel* clean-up process when the best manually selected pattern is chosen as the starting point. Starting pattern consists of two line arrays of *jexels* (four line arrays of jets).

IV. ARE TOO MANY JETS COUNTERPRODUCTIVE FOR EFFECTIVE CONTROL?

In this section, a direct exploration of the question posed at the beginning of this study is performed. A *jexel* is deemed a "negative contributor" in the context of this study when it drives the cost function J away from the goal direction. Therefore, "negative contributors" increase circulation in the flow field of solution and deactivating them would decrease the value of the cost function—decreasing the measured circulation.

A batch of experiments with the intent of "cleaning up" the best manually selected line array configuration was performed according to the algorithm discussed in Sec. III as well as in the Appendix, where both "negative contributors" as well as "noncontributors" are sought to be eliminated. The best manually defined pattern, shown as "Starting Pattern" in Fig. 3, consisted of four line arrays of microjets. Other configurations with line arrays are explored in detail in a previous study [21].

The relative decrease in circulation as measured by the four-hole probe is shown as a function of the number of deactivated *jexels* in Fig. 3. The probe measured circulation around the right-hand vortex core as seen from upstream of the model. The configuration starts with a total of 24 *jexels*, amounting for 96 jets activated. It is worth mentioning that configurations with a single line of *jexels* (i.e., only the line in the cylindrical surface or only the line in the flat part of the slanted surface) were tested, both yielding inferior results ($\Delta\Gamma/\Gamma \sim -2\%$), as shown in Fig. 2(c).

In Fig. 3 the red dots represent the evaluation of the cost function for every *jexel* candidate to be deactivated, and the blue stars represent the *jexel* elected to be deactivated for the next round (outer *for loop* described in the Appendix). The progression of cost function evaluations indicate that deactivating *jexels* of the starting pattern yields a superior performance in terms of circulation reduction, beyond the measurement uncertainty of the four-hole probe. Consistent improvements in circulation reduction occur until there are only four *jexels* active (-20 *jexels*, $\Delta\Gamma/\Gamma = -6.2\%$), after which the performance of the active flow control pattern degrades rapidly as every last *jexel* is deactivated. Curiously, the configuration -20 *jexels* is very similar to the solution found by the GA [Fig. 2(d)], except for its lack of symmetry, as well as the *jexels* that were not active in the starting pattern.

This iterative "clean-up" procedure not only enables one to define which *jexels* were the major contributors for the observed performance, but in this case it also identified *jexels* that are negatively contributing to the performance. This can be asserted because every possible *jexel* was deactivated in each round of this algorithm, and only a subset of *jexels* caused the cost function to improve when

deactivated, at any given round. In the case studied here, one could state that the 20 *jexels* deactivated from the starting pattern to the −20 *jexels* configuration are either hurting the performance or are not contributing to it, which is strong evidence that the line array of jets is not the most optimal configuration in this flow. One can then ask whether similarly problematic microjets are present in other studies that involve line arrays of microjets, and whether this technique could be useful in pinpointing them. The question is of relevance, since reducing the number of jets active while keeping the momentum input for each individual jet constant is crucial to improve the performance of active flow control systems, especially when those microjets are hurting the performance of the flow control strategy.

V. FLOW FIELD CHANGES PROMOTED BY THE GENETIC ALGORITHM SOLUTION

A. Modified surface flow pattern

Since the GA solution seems to be more effective at achieving the cost function of reducing drag than a traditional line array solution, it is worthwhile to understand the physical mechanisms that the GA leveraged so that we can learn what good practices can be incorporated in future flow control studies. Surface flow visualization was performed with a thin layer of light oil with sprinkled fluorescent chalk particles and the pattern was left to develop for about 30 minutes. The very low freestream velocity used in this study ($V_\infty = 10.3$ m/s) made it very challenging to develop the surface flow pattern in certain regions of this flow, where the velocity was lower, leaving some regions of the surface undeveloped. Figure 4 shows the results obtained between the baseline surface oil flow, with no *jexels* active [Fig. 4(a)] and the best solution obtained by the GA [Fig. 4(b)], as well as the best manually selected pattern [Fig. 4(c)], which consisted of four line arrays of microjets.

The baseline solution of Fig. 4(a) displays the features discussed by Zigunov *et al.* [42], with a continuous arc line denoting the footprint of the horseshoe-like vortex that sits atop of the slanted surface, as sketched in Fig. 1(b). The reattachment point of the separation bubble of the baseline case occurs at $s/D = 0.46$, noting that $s = 0$ is located at the leading edge of the slanted surface. It is clear that the line array solution of Fig. 4(c) moved the reattachment point upstream to $s/D = 0.36$, which reduces the size of the suction region under the separation bubble that is responsible for a large contribution to the drag on this model. However, the GA solution in Fig. 4(b) clearly reduced the size of the separation region to a much smaller value ($s/D \approx 0.08$, as will be discussed in Sec. V C), which is very likely the main contributor to the large circulation reduction observed. As the solution found by the GA was not actuating portions of the body further downstream, this solution is probably optimal given the area of coverage of the microjet actuators implemented at the start of the GA study and the limitation of being unable to individually each microjet state. As a side note, enabling the microjets in the GA solution configuration with the wind tunnel running in the baseline configuration will cause the oil flow to shift topologies (Movie 1, scene 1) [48], which is a hallmark of the effectiveness of the GA solution's capacity of controlling this flow.

A noteworthy aspect from the flow physics perspective is the apparent formation of "tornado-like" vortices inside the separation bubble in the GA solution. Tornado-like structures have been observed in volumetric PIV measurements of the "stalled regime" of this wake that occurs in this model at lower Reynolds numbers, where the flow features are large enough to directly observe the "tornado-like" vortices. A direct experimental observation of the "tornado-like" vortices in the "vortex regime" subject of this study is yet to be performed; however, the GA solution appears to have exploited their (potential) presence to arrive at a highly desirable actuator spatial pattern. As indicated by the blue arrows in the inset detail provided in Fig. 4(b), for which further evidence is presented as a Supplemental Material in Movie 1, scene 3.1 [48], the surface pattern produced by the oil circulates around two microjet holes (the black dots at the center of the blue circular arrows in Fig. 4(b) are the holes from which the jets issue from).

This circulation focal point in the surface flow pattern suggests the presence of two tornado-like vortices that are pinned around the microjets. This solution is not straightforward *a priori*. Adding

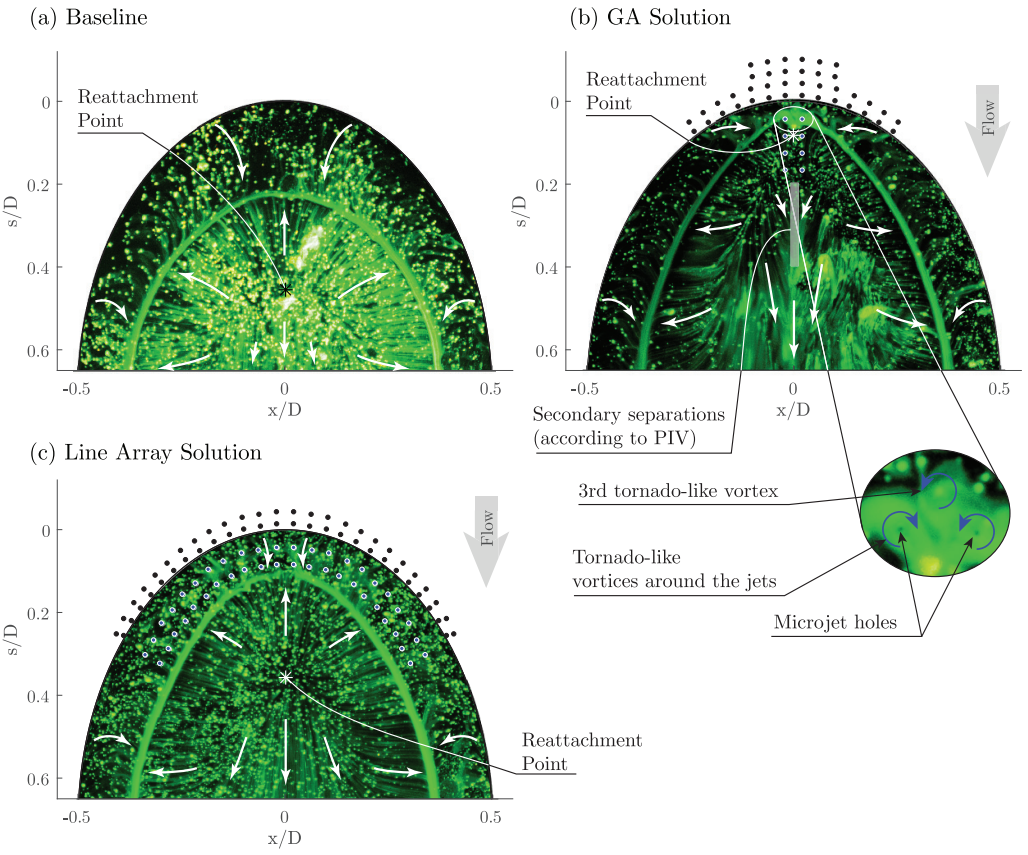

FIG. 4. Comparison between the surface flow patterns generated at $\mathrm{Re}_D = 100\,000$ for baseline (a) and actuated cases (b), (c). Black and blue dots indicate position of the active microjets. Movie 1 in the Supplemental Material [48] clarifies directions given by arrows.

neighboring microjets [as was done in Fig. 4(c)] seems to disrupt this tornado-like vortex formation, making the discovery of this pattern difficult without a system with the flexibility described in this study. It is worth pointing out that in Movie 1, scene 3.1 [48] a third tornado-like vortex is present between the two aforementioned tornado vortices. From the observations made so far, its role in the flow topology is unclear.

Unfortunately, further examination of these very small flow features is very challenging using PIV in a wind tunnel of the size used in the present study. However, given the features observed in surface flow discussed in this section, the authors propose a mechanism for how these two microjets produce the pair of counter-rotating, "tornado-like" vortices: the microjets blowing normal from the slanted surface inside the separation bubble are subject to a relatively quiescent environment, at least near the surface around the first ∼10–15 microjet diameters, where the local velocities are about two orders of magnitude lower than the jet exit velocity. This means the flow field around the jet is similar to the classical problem of the jet in a quiescent flow, where radially inward flow is caused by jet entrainment. Due to the baseline flow already containing some degree of net circulation around the jet axis, the radial inflow causes the formation of a small tornado around it due to conservation of angular momentum. In a sense, the jet acts as a vortex trap similar to a kitchen sink, which means a tornado will form around the jet even if it issued from slightly different locations in the surface, as long as there is net circulation around the jet in the baseline flow. The lowered pressure around

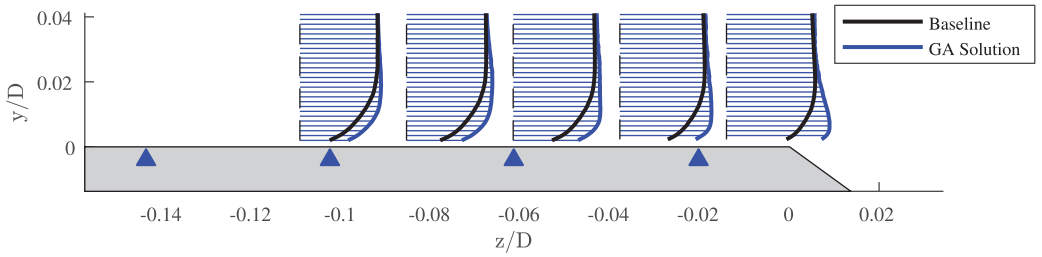

FIG. 5. Comparison between boundary layer V_z profiles as captured by a high-magnification PIV plane at $x = 0$ (centerline, plane b5 in Fig. 1). Blue triangles indicate locations of the microjets closest to the center plane.

the jet, due to both entrainment and the formation of the small tornado, would cause the shear layer above the jets to be pulled towards the slanted surface, shrinking the separation bubble. It is, however, unclear whether the formation of this small tornado is responsible for further pressure lowering around the jet in order to enable this phenomenon. It is possible that the formation of the small tornado-like vortices is simply a secondary effect that manifests itself in the oil flow development but does not cause any appreciable reduction in pressure (with respect to the depression already caused by the jet issuing in the quiescent environment without circulation) to be considered a working principle. It is important to reiterate that no further evidence of the mechanism described in this paragraph was obtained in this study, and if this mechanism plays a role in reducing the size of the separation bubble, it is likely a secondary mechanism.

Nevertheless, the evidence that a nonstraightforward fluid dynamical mechanism can be exploited to shape the wake of a bluff body by tuning the actuators' spatial location should be encouraging in the sense that studies involving patterns other than line arrays can also be highly successful. Finding the effective patterns then becomes the most challenging part of the study that can be enabled with automated approaches.

B. Boundary layer energization

As discussed by Fernandez [2], it is well established that a key working principle of active flow control devices involving microjets in crossflow is the production of a pair of counter-rotating vortices that enhances mixing downstream of the microjets, improving the characteristics of the boundary layer that have the potential to cause massive changes in a flow topology. An examination of the boundary layer characteristics for the GA solution configuration will be presented in this section.

Figure 5 shows the evolution of the states of the boundary layer upstream of the slanted surface as captured by a high magnification PIV setup with a vector spacing of 43.5 μm/vector. Laser reflections near the model surface were mitigated by placing the camera at an angle of -1° with respect to the symmetry plane, which enables the observation of vectors as close to the model surface as $y = 0.28$ mm, with minimal impact in the vertical component of the velocity vectors. Comparing the boundary layer profiles between the baseline case (black lines) and the GA solution (blue lines), it is clear that the microjet actuators energized the boundary layer to a great extent. The boundary layer profile of the baseline case follows a log-law profile at the most upstream station, at $z/D = -0.11$, indicating its development to a turbulent state with a shape factor of 1.5. As the baseline boundary layer evolves downstream, it becomes increasingly energized as a highly favorable pressure gradient is established due to the formation of the suction zone after separation. In the GA solution case where the microjet actuators are turned on, the boundary layer is already highly energized at the most upstream station ($z/D = -0.11$) due to the mixing effect of the microjet upstream at $z/D = -0.144$. However, the boundary layer profiles become increasingly fuller and

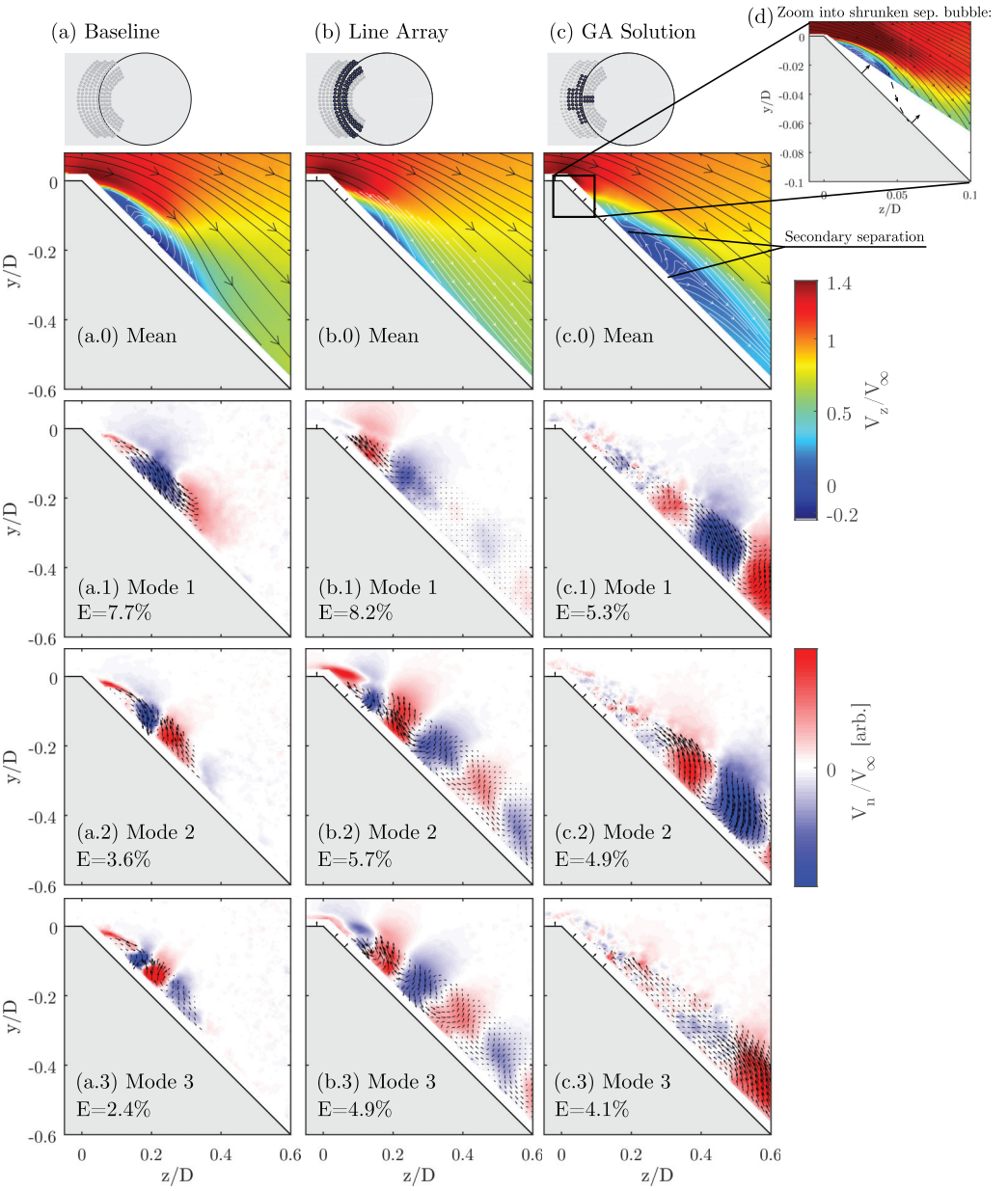

FIG. 6. PIV fields of the separation bubble, observed at $\mathrm{Re}_D = 100\,000$ for baseline (a) and actuated cases (b), (c). Top row shows mean fields of streamwise velocity V_z/V_∞ from 500 snapshots. In (d) a high-magnification PIV resolves the very small separation bubble present in the GA solution case. Highest energy POD modes (1–3) displayed in the subsequent subfigures, colored by velocity normal to the slanted surface (V_n/V_∞).

the profile at the edge of the model exceeds the energy of the free stream. This creates a condition where the flow is more likely to reattach after the sharp edge of this model at $z = 0$, which justifies the massive reduction in the separation bubble size presented in Figs. 4(b) and 6(d).

This significant improvement in the boundary layer properties in the actuated case, from a momentum and resistance to separation perspective, is likely caused by a compounded effect of the four jets in tandem employed by the genetic algorithm at the symmetry plane. To the knowledge of the authors, the effect of multiple microjet-in-crossflow actuators in tandem to energize a boundary layer is not well understood in the context of active flow control.

C. Modified separation bubble and modal changes

Planar PIV was first employed to further examine the flow fields and identify the changes promoted by the GA solution in comparison to the solution involving line arrays. These velocity fields were obtained using the PIV plane (b1) in Fig. 1. Figure 6(a) shows the baseline, unactuated case, where Fig. 6(a.0) displays a colored contour plot of mean streamwise velocity with streamlines superimposed. The baseline case, as discussed in [42], displays a closed separation bubble that generates strong suction on the surface, becoming a major contributor to the form drag at the slant angle of $\phi = 45^{\circ}$. Performing proper orthogonal decomposition (POD) [50] on the 500 PIV fields obtained yields the principal modes displayed in Figs. 6(a.1)–6(a.3), which simply highlight the separation bubble breathing. Higher order modes (5–10), not shown here for brevity, highlight the leading edge shear layer modes, as expected.

The line array actuator configuration, shown in Fig. 6(b), displays the mean and POD decomposition of the separation bubble. Since the PIV window utilized was the same and the separation bubble size shrank about 20% in length, less of the separation bubble is captured, reducing its contribution to the POD modes. However, different from the baseline configuration, in Figs. 6(b.2) and 6(b.3) a conjugate mode pair is observed, known to represent a traveling wave structure [51]. Since the PIV fields captured are not time-resolved, the direction of convection is not clear: it likely that these structures are convecting with the flow, produced by increased unsteadiness of the shrunken separation bubble, but there is also a possibility that these are feedback structures from the wandering of the vortex pair that propagate upstream.

The same type of conjugate mode pair related to a convective structure is observed in the GA solution displayed in Figs. 6(c.1) and 6(c.2). Part of the complex flow topology in the GA solution that is not well resolved in the surface oil flow experiments due to the low speeds can be observed in Figs. 6(c.0) and 6(d). The separation bubble is too small to be captured by PIV due to the laser reflections at the low magnification presented in Fig. 6(c.0), prompting the authors to perform a follow-up experiment with a high magnification lens to resolve this flow structure. As can be observed in Fig. 6(d), the separation bubble has a minute size that is estimated to reattach at $z/D \approx 0.06$, a significant reduction when comparing with the baseline case where the reattachment point is estimated to be at $z/D = 0.33$. However, the flow still does not have sufficient energy to remain reattached in face of the highly adverse pressure gradient downstream of the reattachment point, prompting the flow to separate later downstream at two different locations [indicated as "secondary separation" in Fig. 6(c.0)]. Due to the small sizes and 3D complexity of the modified flow topology, further investigation still needs to be performed to fully understand the phenomena at play.

The modal decomposition of the PIV images from the GA solution case presented in Figs. 6(c.1)–6(c.3) indicates the convective mode then ranks the highest in the decomposition; however, its wavelength is about ∼43% longer than in the linear array solution. Interestingly, this longer wavelength is observed under a much smaller near-surface velocity, displayed in the mean field of Fig. 6(c.0), which is the opposite of what would be expected if they represented the same kind of instability, since the lower convective velocity would decrease the wavelength for a fixed frequency. This suggests the principal mode observed in the GA solution is significantly lower in frequency. The convective velocity of these large scale turbulent structures, however, cannot be reliably defined with the non-time-resolved data set captured. It is also important to note that masking out the separation bubble from the baseline case and reprocessing the POD algorithm does

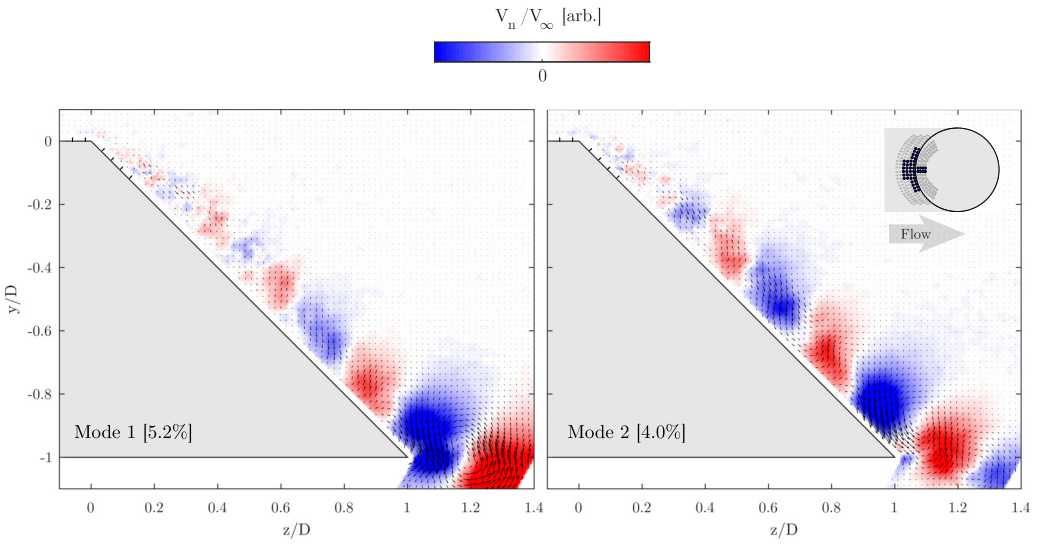

FIG. 7. Principal modes of the GA solution at $\mathrm{Re}_D = 100\,000$ when a larger PIV field is used, displaying a traveling wave pair.

not yield the traveling wave modes observed in Figs. 6(b) and 6(c), meaning they either are not present or are below the PIV correlation noise levels to be detected.

The mode energy, as shown in Fig. 6, peaked at about 5%–8% of the total energy and rapidly decayed, as expected for the POD of a turbulent flow. The energy values, however, are not as significant in the case of experimental PIV fields, since much of the energy contribution is due to correlation noise due to the low dynamic range of the technique.

The convective wave mode pair produced by the GA appears to be an unstable wave, as evidenced by the observations from a second experiment where the PIV field of view was enlarged to include the entire model. This is shown in Fig. 7, where the first two modes are displayed for the GA solution only, since the principal modes of the Baseline case are similar to Fig. 6(a). As can be observed, the second mode observed in the full field PIV is indeed a traveling wave pair [51] and has a qualitatively similar shape, but with a spatial phase shift. This wave extends further into the wake, growing in strength and very likely affecting the vortex pair and increasing its wandering, as will be discussed in Sec. V D 1.

D. Changes promoted to the far field vortex pair

1. Mean far field vortices and vortex wandering

A closer examination at the far field of the wake produced by this model, at $z/D = 2$ was performed with SPIV as described in Sec. II B 1. The mean vorticity field obtained from 500 SPIV snapshots is shown along with the tracked vortex core locations from instantaneous snapshots in Fig. 8. The vertical position of the mean vortex core is significantly moved upwards in the GA solution [Fig. 8(b)] with respect to the baseline solution. This is more clearly observed when focusing on the difference in location between the yellow circle markers placed in Fig. 8(b), which represent the mean core of the baseline case, and the yellow stars, which represent the mean core location of the actuated case. The vertical displacement is, on average, $0.048D$ upwards. The upwards displacement is consistent with the observed reduction in vortex core circulation of $\Delta\Gamma/\Gamma = -10.6\%$, as the lower vortex strength results in reduced induced velocity and an upwards shift in the vortex core location as the vortices convect downstream. The changes promoted by the line array solution were not nearly as dramatic, which is the reason it is not displayed in Fig. 8. They

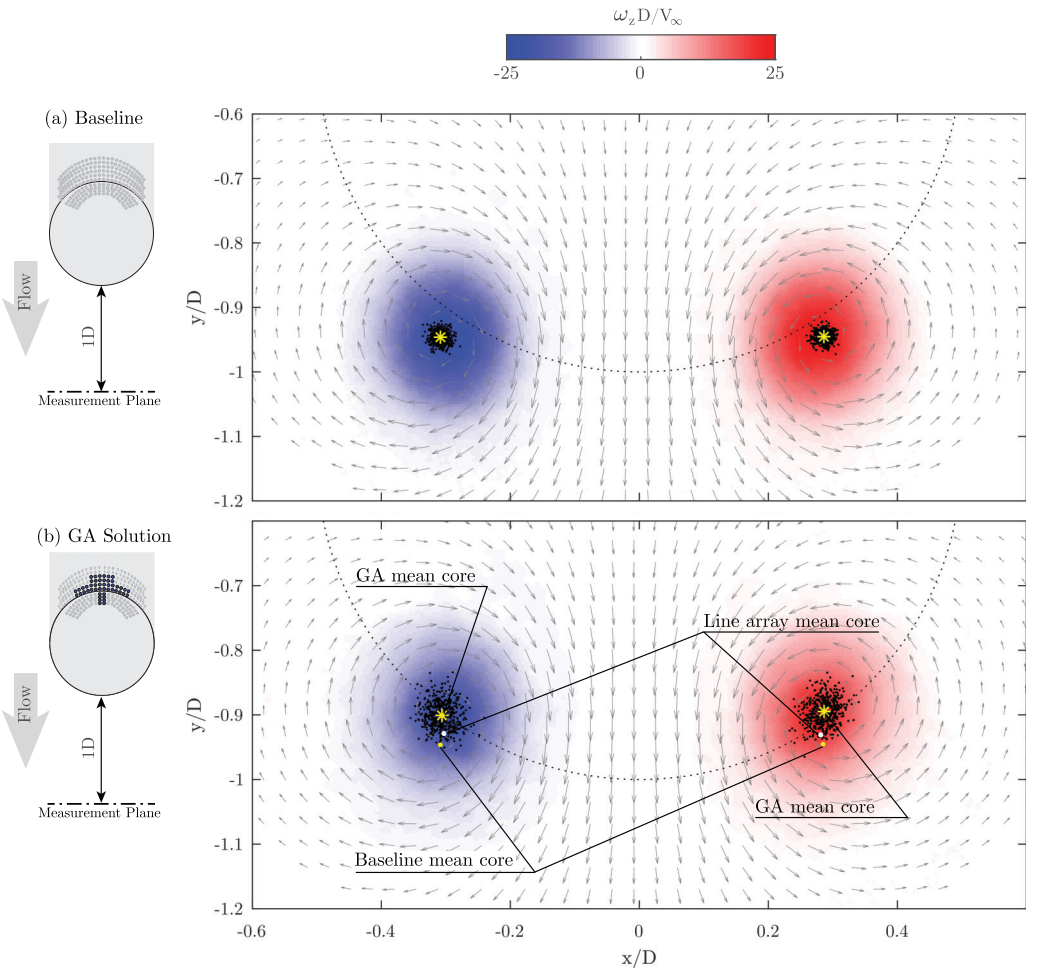

FIG. 8. Mean vorticity fields obtained from 500 SPIV fields at $\mathrm{Re}_D = 100\,000$ and $z/D = 2$. Yellow stars indicate mean vortex core, whereas black dots indicate instantaneous vortex cores as found by peak Γ_1. (b) Baseline and line array mean cores also shown to facilitate comparison between the results. Line array solution omitted due to its high similarity to the baseline field (a).

are reported in Table I for reference. Note that the cost per *jexel*, associated with actuation in terms of actuator size, weight and energy are the same for both cases examined, since the supply pressure $P_S = 52$ kPa and blowing ratio $B = 7.3$ were maintained fixed for both cases. Hence, the number of *jexels* determines the actuation cost in the cases examined, which is higher for the "line array" configuration (24 active *jexels*) than for the "GA solution" configuration (12 active *jexels*).

TABLE I. Changes promoted by each actuation scheme as measured from 500 SPIV fields at $z/D = 2$.

	$\bar{x}_c/D$		$\bar{y}_c/D$		$\sigma_{x,c}/D$		$\sigma_{y,c}/D$				$\Gamma/V_\infty D$		
Case	L	R	L	R	L	R	L	R	$\Delta\sigma_x$	$\Delta\sigma_y$	L	R	$\Delta\Gamma/\Gamma$
Baseline	−0.308	0.286	−0.946	−0.945	0.0092	0.0089	0.0089	0.0082	–	–	0.792	0.796	–
Line array solution	−0.303	0.283	−0.928	−0.930	0.0086	0.0078	0.0096	0.0088	−9.4%	+7.6%	0.765	0.771	−3.3%
GA solution	−0.306	0.287	−0.900	−0.895	0.0174	0.0170	0.0208	0.0202	+90%	+139%	0.712	0.716	−10.6%

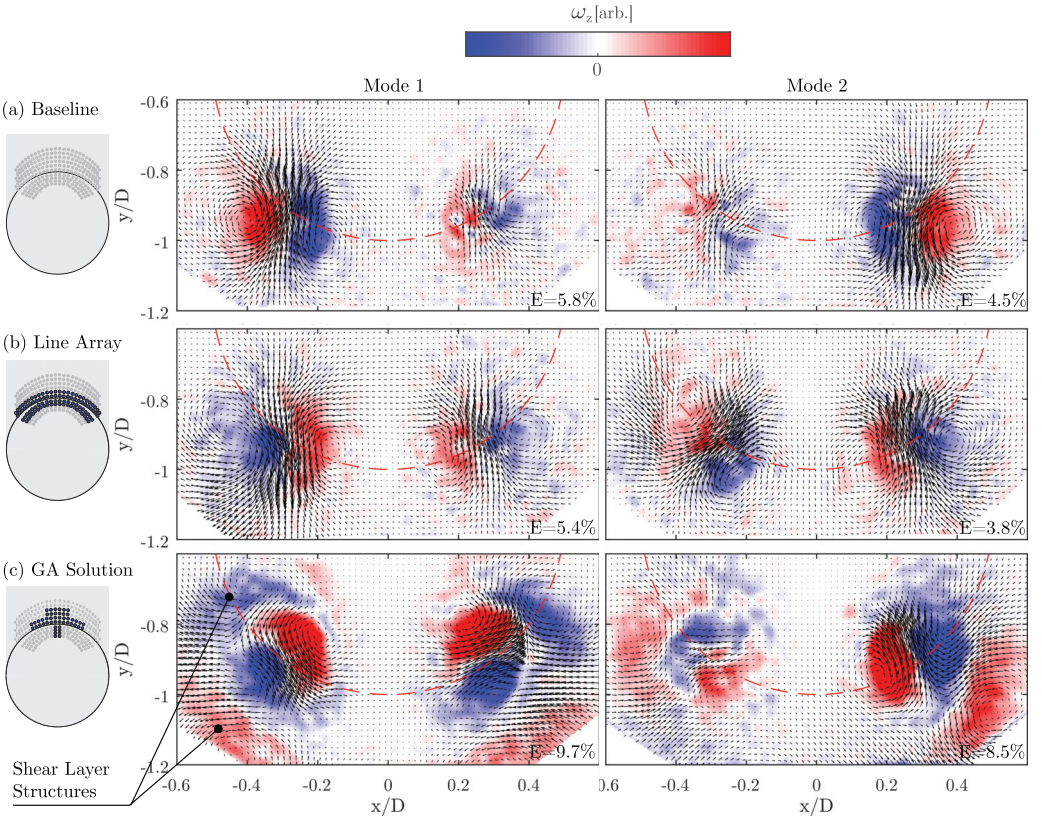

FIG. 9. Two principal vorticity modes of the vortex pair for the three cases studied, acquired from 500 SPIV snapshots at $z/D = 2$.

A greatly increased variability in the position of the tracked vortex core is also observed in the GA solution of Fig. 8(b) when compared to the baseline case (a). The vortex core was tracked by finding the peak of the Γ_1 quantity [52], which geometrically defines the vortex core based on the angle of the vectors and proved to be very effective in suppressing the inherent noise present in instantaneous PIV fields by averaging the contribution of multiple vectors. The standard deviation of the vortex core location $\Delta\sigma = (\sigma_{\text{jets}} - \sigma_{\text{baseline}})/\sigma_{\text{baseline}}$ increased by 90% in the spanwise (x) direction and 139% in the vertical (y) direction, as displayed in Table I. This is much more significant than the changes in wandering promoted by the line array solution, which were of $O(10\%)$, indicating an instability mechanism was potentially triggered by the GA solution.

2. Principal POD modes of the far field vortex pair

A modal decomposition of the 500 SPIV fields captured is presented in Fig. 9. Only the two most energetic modes are displayed for each case, for brevity. It becomes clear in this decomposition that the line array solution of Fig. 9(b) was not able to fundamentally change the modal composition of the flow field when compared with the baseline of Fig. 9(a). Both configurations highlight a component of the first helical mode of each vortex, as opposite vorticity clouds are present around the core of both vortices. However, a similar mode shape and mode energy level is observed for both the line array configuration of Fig. 9(b) and the baseline case [Fig. 9(a)].

This is in contrast to the GA solution, which clearly impacted the principal modes of the vortex pair, as displayed in Fig. 9(c). The effect appears to be related to the increased unsteadiness of the trailing edge shear layer discussed in Sec. V C, as shear layer structures are also energetic enough

now to appear in the first and second modes—meaning they are also correlated with the (possibly low-frequency) vortex core motion. The fluctuation of the shear layer structures at the center line were, unfortunately, not captured due to lack of illumination of the laser sheet at the lower bound of the PIV window. A possible interpretation of this information is that the increased unsteadiness of the shear layer structures wrap around the vortex core as it is convected downstream, increasing unsteadiness around the vortex core and its wandering. If that is indeed the mechanism, it suggests that the solution found by the GA trades off a mean drag reduction for increased unsteadiness in the flow field, which is not necessarily desirable in all engineering applications.

A proposed mechanism for the increased unsteadiness promoted by the GA solution, based on the observations made in this study, is that the decreased size of the separation bubble promoted by the actuation strategy weakens the head of the "horsehoe" vortex structure that manifests itself in the far field as a counter-rotating vortex pair. This weaker connection between the far field vortices reduces the "stiffness" of the low-order dynamical system, enabling them to interact much more strongly with the trailing edge shear layer. It is still not clear, however, if the structures seen in Fig. 7 are a cause of the increased wandering, i.e., they emanate from the shrunken separation bubble and grow unstably downstream, or if they are simply an upstream manifestation of the increased vortex motion downstream due to the trailing edge shear layer instability. Whether this trade-off drag reduction/wake instability is required in bluff body wakes like the model studied is still unclear, although the particular strategy adopted by the GA clearly decreased the stability of the vortex pair.

VI. CONCLUSION

This study explored the solutions found by a genetic algorithm tackling the microjet actuator sensitivity problem with advanced flow diagnostic techniques to explore the physical interactions that resulted in the drag reduction observed. It was found that line arrays are far from an optimal solution in the slanted cylinder wake control problem under the conditions described in this experiment, partly due to many of the microjets constituting the line array being detrimental to the performance of the actuation strategy. Removing 80 out of 96 microjets of a multiline array actuation strategy improved the inferred drag reduction of the strategy from 3.5% to 6.2%, which is clearly beneficial from the complexity and actuation cost standpoints.

Further examining the solution promoted by the genetic algorithm, which reduced the inferred drag by 10.6%, showed the strategy leveraged the well-known counter-rotating vortex pair produced by multiple microjet in crossflow arranged in tandem to energize the boundary layer upstream of separation with great effectiveness. The GA preferentially selected particular positions of microjets near the symmetry plane where the boundary layer energization was most effective in changing the topology of the separation bubble formed downstream of the model edge, a strategy that is not straightforward even to an experienced researcher. Furthermore, a set of eight jets that were previously immersed inside the separation bubble had a crucial role in maintaining this flow topology; however, it was not possible to identify the precise mechanism through which this was effected.

Finally, particle image velocimetry observations show that the actuation strategy encountered by the GA trades an increased unsteadiness (about twice as much with respect to the baseline) of the far field vortex pair for an improvement in form drag, which seems to be related to its natural helical instability. This unstable mode appears to exhibit coupling with the instability of the shear layer produced by the trailing edge after a reduction in size of the separation bubble. It is encouraging to observe that complex fluid dynamic phenomena can effectively be leveraged by experimental machine learning approaches, even when the details of the flow physics are not completely well understood.

ACKNOWLEDGMENTS

This research is supported by the Air Force Office for Scientific Research (AFOSR), Grant no. FA9550-17-1-0228, "Dynamics of Unsteady Flow Past Bluff Bodies with Lofted Bases." The authors would like to thank Prof. Datta Gaitonde and Dr. Rajesh Ranjan for insightful discussions.

Furthermore, the authors would also like to thank the master machinist Jeremy Phillips for his expertise and craftsmanship in preparing the actuator parts required for this study.

APPENDIX

1. Details of the genetic algorithm implementation

The particular implementation of the GA used in this study defined a case genome with one continuously varying parameter for the *jexel* supply pressure, $0 < P_S < 70$ kPa, and four arrays of parameters of variable length: *JxAddresses* stores the addresses (1–59) of the *jexels* activated for that case; *JxPhases* stores the individual phase delays with respect to a reference time, *JxDuties* stores the duty cycle used for each *jexel*. A single frequency, *JxFrequency*, was used for all *jexels*. All arrays had the same length, which corresponded to the number of *jexels* activated for the corresponding case. A minimum length of five and a maximum length of 25 was defined, limited by the maximum current capacity of the electronic board designed.

The GA was then fed an initial population of 30 *jexel* configurations, which were the best cases obtained after a parametric scan of manually selected patterns that followed the classical "informed *ad hoc*" approach. These patterns are further detailed in [21]. The population was kept constant at 30 individuals per generation. For each individual, the cost function described in Eq. (1) was measured and evaluated.

The baseline circulation, Γ_{baseline}, was reevaluated with all *jexels* deactivated after every 10 cases to make sure any low-frequency trends in the baseline case were mitigated. A moving average of 10 baselines was used to reduce sudden changes between the individuals' cost functions.

Every generation, the genetic algorithm performed the operations described below. The specific values of the probabilities and probability distributions were arbitrary and were kept unchanged during the experiment:

Elitism: 40% (12) of the best individuals (least J) were selected as "elite" individuals and carried over to the next generation.

Mutation: Each elite individual was then mutated. Mutation would perform the following operations:

Change jexel count: With a probability of 30%, the number of *jexels* would be changed. If change occurred, one *jexel* would be added to or removed from all arrays with 50% chance.

Change jexel addresses: With a probability of 30%, the addresses of N *jexels* would be changed. The random number N, between 1 and 6, would be picked from a uniform distribution and random entries of the *JxAddresses* array would be swapped to unassigned addresses.

Change jexel frequency: With a probability of 50%, the frequency f of all *jexels* would be added to a Gaussian random number of zero mean and standard deviation of 30 Hz. To ensure $0 \leqslant f \leqslant 200$ Hz, another random number would be picked if the frequency was out of bounds until $0 \leqslant f \leqslant 200$ Hz.

Change jexel phases: With a probability of 50%, the phases of N *jexels* would be changed. The random number N, between 1 and 6, would be picked from a uniform distribution and random entries of the *JxPhases* array would be added to a Gaussian random number of zero mean and standard deviation of 60°. Proper phase wrapping was performed.

Change jexel duty cycles: With a probability of 50%, the duty cycles of N *jexels* would be changed. The random number N, between 1 and 6, would be picked from a uniform distribution and random entries of the *JxDuties* array would be added to a Gaussian random number of zero mean and standard deviation of 30%. The duty cycle was enforced to be between 0 and 100%.

Change supply pressure: With a probability of 30%, the backpressure P_S of all *jexels* would be added to a Gaussian random number of zero mean and standard deviation of 20 kPa. To ensure $0 \leqslant P_S \leqslant 70$ kPa, another random number would be picked if the supply pressure was out of bounds.

Crossover: The remainder 60% (18) individuals were "children" of the mutated elite individuals generated with the two previous steps. Crossover would be performed by following the steps below:

Choose parents: Two random individuals from the 12 mutated elite individuals would be selected for the crossover operation.

Jexel count definition: Since each parent is expected to have a different number of *jexels*, one of the parents was picked randomly, with equal probability, to define the length of the child's genome (i.e., the length of the *JxXXX* arrays).

Crossover jexels: The genome of the selected parent was copied to the child's genome. Then, half of the *jexels* would be randomly selected and swapped by the other parent's *jexels*. Nonrepeatability of the *jexel* addresses was enforced.

Supply pressure interpolation: The supply pressure was interpolated between the two parents with a randomly chosen weight $0 < w < 1$, such that $P_{B,C} = wP_{B,P1} + (1 - w)P_{B,P2}$.

Evaluation: All the new individuals in the current generation would be evaluated by measuring Γ and computing J.

This algorithm was performed every generation. From generation 30 onwards, however, in order to prevent the aggressively random parameters from changing the population too much, the best three elite individuals stopped being mutated by the algorithm.

2. Details of the *jexel* clean-up procedure

The inherent randomness of the GA is known to produce results that are difficult to interpret. To improve interpretability and draw better conclusions about what the solution found by the GA is doing, a clean-up procedure was performed after convergence of the GA. This clean-up procedure is necessary because there could be many *jexels* in the best configurations that do not have a significant effect on the cost function, but did not get removed by the GA due to random chance or the limitation in the number of iterations performed. This step, therefore, is crucial to draw a deeper understanding from the results.

Starting with the "BestIndividual" configuration, the following pseudocode was used:

```
CurrentIndividual ← BestIndividual;
for j ← 1 to BestIndividual.nJexels do
    for i ← 1 to CurrentIndividual.nJexels do
        TestIndividual ← CurrentIndividual;
        TestIndividual.RemoveJexel(i);
        Cost(i)=TestIndividual.EvaluateCostFunction();
    end
    Find K that minimizes Cost(K);
    CurrentIndividual.RemoveJexel(K);
end
```

Following this procedure enabled assessment of the contribution of each individual *jexel* to the obtained solution, slowly removing one *jexel* at a time and observing how relevant its contribution was. As discussed in Sec. IV, many of the *jexels* produced by the GA could be removed without reducing the solution fitness, unveiling a reasonably interpretable pattern.

[1] L. N. Cattafesta and M. Sheplak, Actuators for active flow control, Annu. Rev. Fluid Mech. **43**, 247 (2011).

[2] E. Fernandez, On the properties and mechanisms of microjet arrays in crossflow for the control of flow separation, Ph.D. thesis, Florida State University, 2014.

[3] F. Schlegel, D. Wee, Y. M. Marzouk, and A. F. Ghoniem, Contributions of the wall boundary layer to the formation of the counter-rotating vortex pair in transverse jets, J. Fluid Mech. **676**, 461 (2011).

[4] H. Park, J.-H. Cho, J. Lee, D.-H. Lee, and K. H. Kim, Experimental study on synthetic jet array for aerodynamic drag reduction of a simplified car, J. Mech. Sci. Tech. **27**, 3721 (2013).
[5] M. Metka and J. W. Gregory, Drag reduction on the 25-deg Ahmed model using fluidic oscillators, J. Fluids Eng. **137**, 051108 (2015).
[6] P. Joseph, X. Amandolese, and J.-L. Aider, Drag reduction on the 25° slant angle Ahmed reference body using pulsed jets, Exp. Fluids **52**, 1169 (2012).
[7] J. McNally, N. Mazellier, F. Alvi, and A. Kourta, Control of salient flow features in the wake of a 25-deg Ahmed model using microjets, Exp. Fluids **60**, 7 (2018).
[8] R. Jackson, Z. Wang, and I. Gursul, Control of upswept afterbody vortices using continuous and pulsed blowing, J. Aircr. **57**, 76 (2020).
[9] V. H. Arakeri, A. Krothapalli, V. Siddavaram, M. B. Alkislar, and L. M. Lourenco, On the use of microjets to suppress turbulence in a Mach 0.9 axisymmetric jet, J. Fluid Mech. **490**, 75 (2003).
[10] T. J. Worden, P. Upadhyay, J. P. R. Gustavsson, and F. S. Alvi, Studies on microjet control effectiveness in high-temperature supersonic impinging jets, AIAA J. **52**, 1757 (2014).
[11] J. Gavin, E. Fernandez, P. Sellappan, F. Alvi, W. Bilbow, and S. Xiang, Implementing rotating stall control in a radial diffuser using microjet arrays, in *Active Flow and Combustion Control 2018*, Notes on Numerical Fluid Mechanics and Multidisciplinary Design, Vol. 141, edited by R. King (Springer, New York, 2018).
[12] K. S. Aley, T. K. Guha, and R. Kumar, Active flow control of a high-lift supercritical airfoil with microjet actuators, AIAA J. **58**, 1 (2020).
[13] F. A. E. F. J. G. Joost Brasz, William Bilbow, Active surge control in centrifugal compressors using microjet injection, US Patent US20190040865A1 (2016).
[14] A. M. Ruiz, G. Lacaze, and J. C. Oefelein, Flow topologies and turbulence scales in a jet-in-cross-flow, Phys. Fluids **27**, 045101 (2015).
[15] S. Bhaumik, D. V. Gaitonde, S. Unnikrishnan, A. Sinha, and H. Shen, Verification and application of a mean flow perturbation method for jet noise, Aerosp. Sci. Technol. **80**, 520 (2018).
[16] A. Uzun, T. B. Davis, F. S. Alvi, and M. Y. Hussaini, Optimally growing boundary layer disturbances in a convergent nozzle preceded by a circular pipe, Theor. Comput. Fluid Dyn. **31**, 317 (2017).
[17] C.-A. Yeh and K. Taira, Resolvent-analysis-based design of airfoil separation control, J. Fluid Mech. **867**, 572 (2019).
[18] J. H. Marques Ribeiro, C.-A. Yeh, and K. Taira, Randomized resolvent analysis, Phys. Rev. Fluids **5**, 033902 (2020).
[19] Y. Sun, Q. Liu, L. N. Cattafesta III, L. S. Ukeiley, and K. Taira, Resolvent analysis of compressible laminar and turbulent cavity flows, AIAA J. **58**, 1046 (2020).
[20] Q. Liu, Y. Sun, C.-A. Yeh, L. S. Ukeiley, L. N. Cattafesta III, and K. Taira, Unsteady control of supersonic turbulent cavity flow based on resolvent analysis, arXiv:2003.10091 [physics.flu-dyn].
[21] F. Zigunov, P. Sellappan, and F. S. Alvi, An empirical platform for optimal placement of open-loop microjet-in-crossflow actuators, in *AIAA Scitech 2021 Forum* (AIAA, Reston, VA, 2021).
[22] N. Vandelli, D. Wroblewski, M. Velonis, and T. Bifano, Development of a MEMS microvalve array for fluid flow control, J. Microelectromech. Syst. **7**, 395 (1998).
[23] E. Fernandez, V. Kumar, R. Kumar, and F. Alvi, Active separation control on highly loaded LPT blades using microjets, in *48th AIAA Aerospace Sciences Meeting Including the New Horizons Forum and Aerospace Exposition* (AIAA, Reston, VA, 2010).
[24] V. Kumar and F. S. Alvi, Use of high-speed microjets for active separation control in diffusers, AIAA J. **44**, 273 (2006).
[25] L. Mears, N. Arora, and F. Alvi, Flowfield response to controlled perturbations in swept shock/boundary-layer interaction using unsteady PSP, in *AIAA Scitech 2019 Forum* (AIAA, Reston, VA, 2019).
[26] B. L. O. Ramos, W. R. Wolf, C.-A. Yeh, and K. Taira, Active flow control for drag reduction of a plunging airfoil under deep dynamic stall, Phys. Rev. Fluids **4**, 074603 (2019).
[27] E. A. Deem, Flow physics and nonlinear dynamics of separated flows subject to ZNMF-based control, Ph.D. thesis, Florida State University, 2018.

[28] P. Joseph, X. Amandolese, C. Edouard, and J.-L. Aider, Flow control using MEMS pulsed micro-jets on the Ahmed body, Exp. Fluids **54**, 1442 (2013).
[29] P. Joseph, D. Bortolus, and F. Grasso, Flow control on a 3D backward facing ramp by pulsed jets, CR Mécanique **342**, 376 (2014).
[30] D. Barros, T. Ruiz, B. Jacques, and B. Noack, Control of a three-dimensional blunt body wake using low and high frequency pulsed jets, Int. J. Flow Control **6**, 61 (2014).
[31] J. Wilson, D. Schatzman, E. Arad, A. Seifert, and T. Shtendel, Suction and pulsed-blowing flow control applied to an axisymmetric body, AIAA J. **51**, 2432 (2013).
[32] J. McNally, E. Fernandez, G. Robertson, R. Kumar, K. Taira, F. Alvi, Y. Yamaguchi, and K. Murayama, Drag reduction on a flat-back ground vehicle with active flow control, J. Wind Eng. Ind. Aerodyn. **145**, 292 (2015).
[33] Y. Zhang, Y. Sun, N. Arora, L. N. Cattafesta III, K. Taira, and L. S. Ukeiley, Suppression of cavity flow oscillations via three-dimensional steady blowing, AIAA J. **57**, 90 (2019).
[34] G. T. K. Woo, A. Glezer, S. Yorish, and T. M. Crittenden, Pulsed actuation control of flow separation on a ROBIN rotorcraft fuselage, AIAA J. **54**, 3274 (2016).
[35] A. Wortman, Reduction of fuselage form drag by vortex flows, J. Aircr. **36**, 3 (1999).
[36] N. Gautier, J.-L. Aider, T. Duriez, B. Noack, M. Segond, and M. Abel, Closed-loop separation control using machine learning, J. Fluid Mech. **770**, 442 (2015).
[37] A. Debien, K. A. F. F. Krbek, N. Mazellier, T. Duriez, L. Cordier, B. R. Noack, M. W. Abel, and A. Kourta, Closed-loop separation control over a sharp edge ramp using genetic programming, Exp. Fluids **57**, 40 (2016).
[38] T. Duriez, B. Steven, and B. Noack, *Machine Learning Control—Taming Nonlinear Dynamics and Turbulence* (Springer International Publishing, Switzerland, 2017).
[39] T. Morel, Effect of base slant on flow in the near wake of an axisymmetric cylinder, Aeronaut. Quarterly **31**, 132 (1980).
[40] F. Zigunov, Detailed flow field study of an upswept cylinder wake and experimental optimization using active flow control, Ph.D. thesis, Florida State University, 2020.
[41] D. J. Garmann and M. R. Visbal, High-fidelity simulations of afterbody vortex flows, AIAA J. **57**, 3980 (2019).
[42] F. Zigunov, P. Sellappan, and F. S. Alvi, Reynolds number and slant angle effects on the flow over a slanted cylinder afterbody, J. Fluid Mech. **893**, A11 (2020).
[43] M. T. Aultman, R. Ranjan, and D. V. Gaitonde, Effect of upsweep angle on the mean flowfield of a simulated cargo fuselage, in *AIAA Scitech 2020 Forum* (AIAA, Reston, VA, 2020).
[44] D. S. Bulathsinghala, R. Jackson, Z. Wang, and I. Gursul, Afterbody vortices of axisymmetric cylinders with a slanted base, Exp. Fluids **58**, 60 (2017).
[45] R. Ranjan and D. Gaitonde, Hysteresis in slanted-base-cylinder afterbody flows, Aerosp. Sci. Technol. **106**, 106138 (2020).
[46] Y. Bury, T. Jardin, and A. Klöckner, Experimental investigation of the vortical activity in the close wake of a simplified military transport aircraft, Exp. Fluids **54**, 1524 (2013).
[47] F. Zigunov, P. Sellappan, and F. S. Alvi, Dynamics of the slanted cylinder afterbody vortices, in *AIAA Scitech 2020 Forum* (AIAA, Reston, VA, 2020).
[48] See Supplemental Material at http://link.aps.org/supplemental/10.1103/PhysRevFluids.6.083903 for oil flow development time lapses for cases tested.
[49] F. Zigunov, 3dfernando/Jexel-Driver: Jexel Driver-108 count solenoid driver (2020), doi: 10.5281/zenodo.3991588.
[50] G. Berkooz, P. Holmes, and J. L. Lumley, The proper orthogonal decomposition in the analysis of turbulent flows, Annu. Rev. Fluid Mech. **25**, 539 (1993).
[51] K. Taira, S. L. Brunton, S. T. M. Dawson, C. W. Rowley, T. Colonius, B. J. McKeon, O. T. Schmidt, S. Gordeyev, V. Theofilis, and L. S. Ukeiley, Modal analysis of fluid flows: An overview, AIAA J. **55**, 4013 (2017).
[52] L. Graftieaux, M. Michard, and N. Grosjean, Combining PIV, POD and vortex identification algorithms for the study of unsteady turbulent swirling flows, Meas. Sci. Technol. **12**, 1422 (2001).